Solid Freeform Fabrication 2022: Proceedings of the 33rd Annual International Solid Freeform Fabrication Symposium – An Additive Manufacturing Conference
Reviewed Paper

THE EFFECT OF HEAT TREATMENT ON THE MICROSTRUCTURE AND TENSILE PROPERTIES OF LASER POWDER BED FUSED (L-PBF) HAYNES 214

Shaharyar Baig[1,2], Shuai Shao[1,2], Paul R. Gradl[3], Nima Shamsaei[1,2*]

[1] Department of Mechanical Engineering, Auburn University, Auburn, AL 36849, USA

[2] National Center for Additive Manufacturing Excellence (NCAME), Auburn University, Auburn, AL 36849, USA

[3] NASA Marshall Space Flight Center, Propulsion Department, Huntsville, AL 35812, USA

*Corresponding author:
Email: shamsaei@auburn.edu
Phone: (334) 844 4839

Abstract

The as-fabricated microstructure of Haynes 214 by laser powder bed fusion (L-PBF) is dendritic due to the high cooling rates, which is generally considered undesirable and removed via heat treatments. In this study, the effects of various heat treatments on the microstructure and tensile properties of laser powder bed fused Haynes 214 are investigated. Test specimens were fabricated on a L-PBF system in the vertical orientation. Multi-step heat treatments were performed including stress-relief, hot isostatic pressing, solution annealing and ageing. Examining the microstructures revealed columnar grains in the non-heat treated (NHT) condition with grain growth occurring after stress relief. Room temperature tensile tests showed the lowest strengths in the NHT condition. The highest strengths were seen in the aged condition which was attributed to gamma prime precipitation hardening. Finally, the tensile fracture surfaces indicated ductile failure mode in both the NHT and heat treated conditions with the measured elongation being the highest for NHT and lowest in the aged condition.

Keywords: Additive manufacturing (AM), laser powder bed fusion (L-PBF), Haynes 214, microstructure, tensile properties

Introduction

Ni-based superalloys are commonly used in oxidizing environments due to their ability to retain strength, even at elevated temperatures [1–3]. For γ- γ' Ni-based alloys, the main strengthening results from the γ-solid solution consisting of various alloying elements as well as the formation of γ' phase and grain boundary (GB) carbide precipitates at elevated temperatures [3–5]. In the case of Haynes 214 Ni-based superalloy, the addition of Cr and Al allows protective layers of oxides scales to form on the surface which provides resistance to carburizing, nitriding, and corrosion in harsh environments [6]. However, the high content of Al in this alloy typically makes it susceptible to strain-age cracking, especially during any post-process treatments, where the formation of coarse γ' can lead to a stressed microstructure and makes conventional processing challenging [7–9].

Additive manufacturing (AM) looks to be a promising technology to fabricate functional parts as it minimizes the risk of introducing any defects from post-process treatments [9]. Moreover, AM allows the fabrication of complex assemblies, whereby several assembly parts can be fabricated into one integral component [10]. Due to their unique thermal history, the non-heat treated microstructures of AM parts are not only different from their wrought counterparts, but can also vary among different AM technologies [11]. Note that existing heat treatment (HT) schedules available in literature were established for wrought Haynes 214 [9,12]. These HT routines may not result in consistent microstructures and optimized mechanical properties in L-PBF Haynes 214 parts. As such, further studies are required to examine the effect of different heat treatments on the resulting mechanical properties and establish process-structure-property relationship for L-PBF Haynes 214.

In this study, the microstructure and tensile properties of additively manufactured Haynes 214 processed through laser powder bed fusion (L-PBF) are examined. The microstructures in the NHT as well as various solution annealed (SA) only and solution annealed + aged (SA + A) conditions were characterized to identify which conditions may be the most favorable in providing acceptable tensile properties. Room temperature tensile testing was then performed on a few selected conditions as well as the fracture mechanisms were investigated.

Experimental Procedure

Specimens were fabricated using argon-atomized Haynes 214 powder supplied by Praxair technologies with the chemical composition shown in Table 1. The build consisted of vertically oriented specimens processed using the core L-PBF parameters presented in Table 2. A near net-shape geometry was adopted for the as-fabricated samples as can be seen in Figure 1 (a), which would later be cut and/or machined into the final coupon and specimen geometries for microstructural and mechanical characterization, respectively.

Table 1. Chemical composition of Haynes 214 feedstock powder used for fabrication.

Element	Ni	Cr	Al	Fe	Si	Co	Y
Wt. %	Bal.	15.7	4.32	2.36	0.02	0.02	0.01

Table 2. L-PBF Haynes 214 core process parameters used in this study.

Laser Power (W)	**Laser speed (mm/s)**	**Layer Thickness (µm)**	**Hatch distance (µm)**
200	1000	40	70

Cylindrical microstructural coupons, 5 mm in thickness, were excised from the as-fabricated specimens. Some of the microstructural coupons were heat treated, as explained later in this section, to examine the microstructure under various conditions. The coupons were mounted in epoxy resin in the transverse direction (TD), to investigate the microstructure in the plane parallel to the build direction (BD), and ground and polished to a mirror finish. The remaining tensile specimens were surface machined, to reduce any effects of surface roughness resulting from the L-PBF process. The final tensile test specimen geometry is shown in Figure 1 (b).

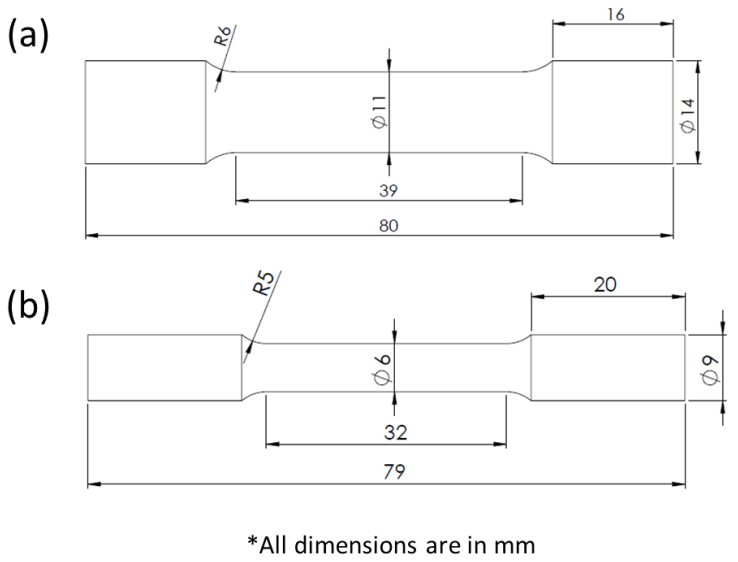

Figure 1. (a) As-fabricated specimen geometry and (b) final tensile test specimen geometry after machining.

All stress relief (SR), solution anneal, and ageing treatments were performed in a Thermo Scientific box furnace. Various multi-step heat treatments were investigated and a list of all heat treatment steps with their associated temperatures, times, and cooling methods are summarized in Table 3. All heat treated specimens were stress relieved in the first step at 1095°C for 2h followed by a hot isostatic pressing (HIP) at 1163°C/100 MPa for 3.5h. The HIP specimens were then solution annealed at 1100°C for 2h as the next step and some of the specimens underwent a final heat treatment step of ageing at 788°C for 8h. Microstructural characterization was performed between each heat treatment step, and three conditions were selected for tensile specimens, namely: NHT, SR+HIP+SA1100 (which is simplified as the SA condition from hereon) and SR+HIP+SA1100+A788 (simplified as the SA + A condition from hereon).

Table 3. Heat treatment conditions with their respective temperatures, pressures, times, and cooling methods.

Heat treatment step	Temperature/Pressure/Time	Cooling method
Stress Relief (SR)	1095°C/Ambient/2h	Furnace cool
Hot Isostatic Press (HIP)	1163°C/100MPa/3.5h	Furnace cool
Solution Anneal (SA)	1100°C/Ambient /2h	Water quench
Age (A)	788°C/Ambient /8h	Water quench

Optical microscopy was performed on polished coupon cross sections using a Keyence VHX 6000 for porosity measurements. The Keyence software was used for analysis of the optical micrographs by setting the thresholds to allow the overall porosity content as well as the size and the geometric features for the defects to be measured. For microstructural characterization, the grain size and morphology were evaluated using a Zeiss Crossbeam 550 scanning electron microscope (SEM) equipped with an electron backscatter diffraction (EBSD) detector. A backscattered electron (BSE) detector was also used to collect images for further microstructural characterization using the SEM.

Tensile testing was performed on an MTS servohydraulic load frame with a load cell capacity of 100 kN. Room temperature tensile testing was conducted according to ASTM E8 under displacement control mode at a strain rate of 0.01 s^{-1}. An extensometer was attached to the specimens for the first 0.035 mm/mm of strain in order to measure the modulus and 0.2% yield strength. For each condition, at least 2 tests were performed and the average values for all of the properties measured were reported. Tensile tests were concluded upon fracture and all fractured specimens were carefully preserved to measure the elongations and reduction in areas as well as to examine the fracture surfaces.

Results and Discussion

The average density, based on optical defect analysis, was measured as 99.88% for the NHT condition. After SR and the HIP cycle, no significant changes were seen in the density value, which was measured to be 99.881%. The histogram of defect size distribution is presented in Figure 2 which shows there were no defects measured larger than 30µm in the HIP condition. This indicates that HIP was able to shrink some of the larger defects however did not significantly affect some of the smaller gas-entrapped pores which were still largely present and observed for both NHT and the specimens which underwent the HIP cycle.

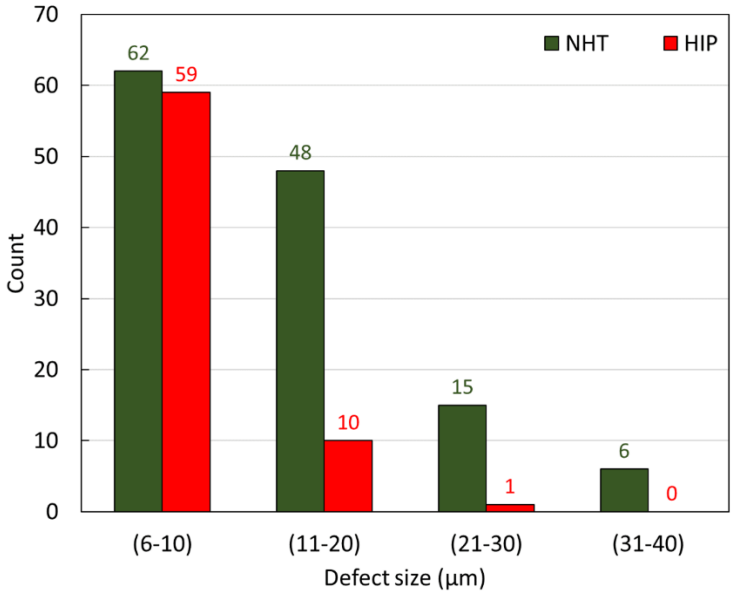

Figure 2. Porosity size distribution for the NHT and HIP specimens.

Figure 3 (a)-(d) presents the inverse pole figure (IPF) plots in the transverse plane for the various heat treated conditions. The average grain sizes for the NHT, SR, SA and SA+A were measured as 24.4 µm, 22.7 µm, 25.4 µm and 24.8 µm, respectively. It can be observed in Figure 3 (a) that in the NHT condition, the grains are columnar and oriented in the build direction. This type of grain structure can be attributed to the epitaxial grain growth enabled by the repeated, layer-by-layer melting-solidifying process, characteristic to the L-PBF process. Such microstructures may not be desirable in load bearing applications as it leads to mechanical anisotropy. After SR, the grain morphology changes significantly with the grains becoming more

equiaxed as shown in Figure 3 (b). The presence of equiaxed grains as well as the higher volume fraction of high angle grain boundaries (i.e., average misorientation angles >10° measured as 40% for NHT and 80% for SR) indicates that significant grain growth has occurred when the specimens were subjected to elevated temperatures of 1065°C during the SR treatment. No further changes were observed in the grain size and morphology after the SA and SA+A treatments as shown in Figure 3(c)-(d).

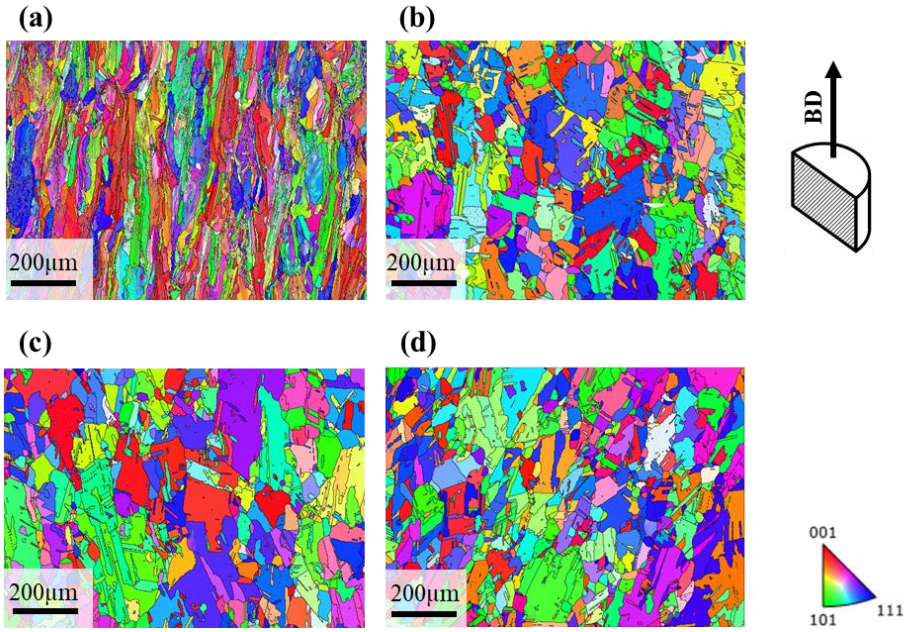

Figure 3. IPF plots in the TD for (a) NHT; (b) SR; (c) SA and (d) SA+A conditions.

Figure 4. presents the BSE micrographs in the transverse plane for the NHT, SA and SA+A specimens. A dendritic microstructure was observed in the NHT condition which results from fast solidification under the high cooling rates inherent to the L-PBF process. After subsequent SR followed by SA at 1100°C for 2h and water quenching, this structure dissolved, and only Al-rich phases (suspected to be topologically close-packed (TCP) intermetallics) could be seen as shown in Figure 4 (d). Heating the specimens to above the solvus temperature of γ' (i.e., 955°C) allowed any precipitates which may have formed during the SR step, to dissolve into the Ni-based matrix resulting in a γ solid solution. The final ageing step at 788°C for 8h resulted in the formation of fine γ' precipitates as well as GB carbides as presented in Figure 4 (e)-(f). It is important to note that the rate of cooling during each heat treatment is critical in determining the amount of age-hardening observed, as γ' can precipitate in Haynes 214 in the temperature range of 595-925°C [9]. Interestingly, no cracks were observed in the SEM micrographs for either the NHT, SA or SA+A conditions. This can be attributed to the Al content for the feedstock powder measured at 4.32 wt.%, which is below the 4.5 wt.% commonly believed to make these alloys non-weldable and thus affecting their processability through AM [13].

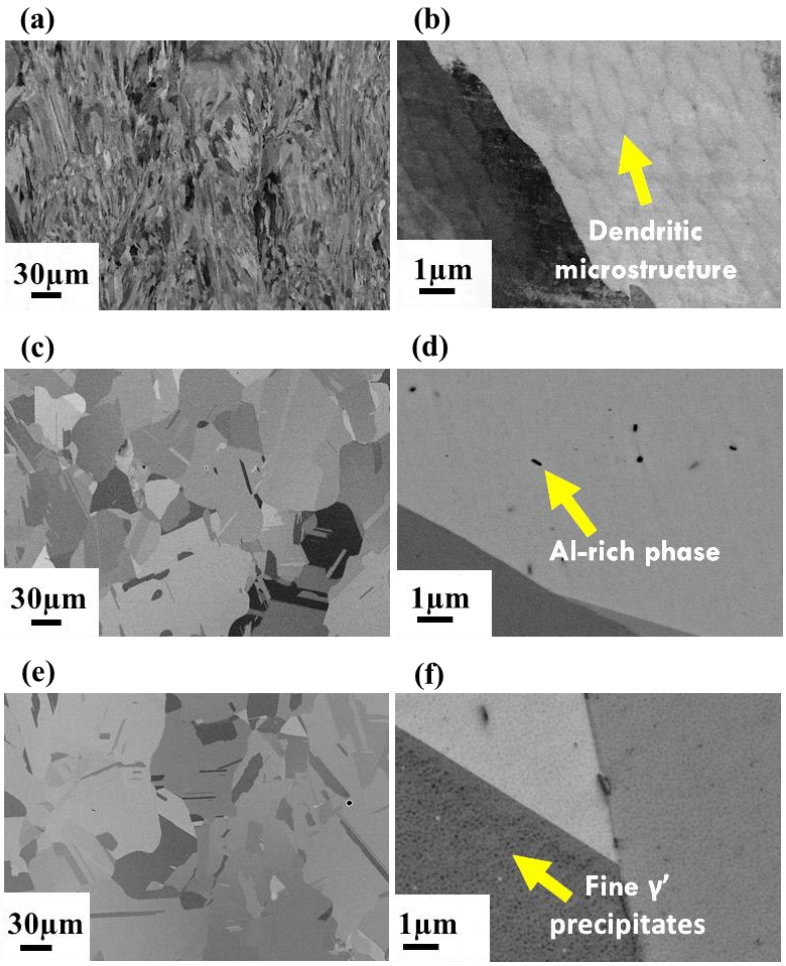

Figure 4. BSE micrographs taken in the TD for (a)-(b) NHT; (c)-(d) SA and (e)-(f) SA+A conditions.

A summary of the measured tensile properties is presented in Figure 5. The elastic moduli were measured as 165, 220 and 221 GPa for the NHT, SA and SA+A specimens, respectively, indicating that significant changes in the phase compositions occurred during heat treatments. In the NHT condition, the yield and ultimate strengths were measured as 516 MPa and 714 MPa, respectively, with a significant amount of necking observed at failure. This is also reflected in Figure 6 (a) which shows a large reduction in the cross-sectional area of the gauge section for the NHT specimen. SR followed by SA resulted in solid solution strengthening which improved the ultimate tensile strength (Su) to 934 MPa, however no significant increase in the yield strength (Sy) was observed, which was measured as 524 MPa. After the ageing treatment, both the yield and the ultimate tensile strengths increased to 618 MPa and 1033 MPa, respectively, which was also accompanied by a reduction in the measured elongation. This can be attributed to the formation of fine γ' precipitates during the ageing process which improved the strengths, however the presence of GB carbides may have led to a reduction in the ductility, as they can serve as early crack initiation sites.

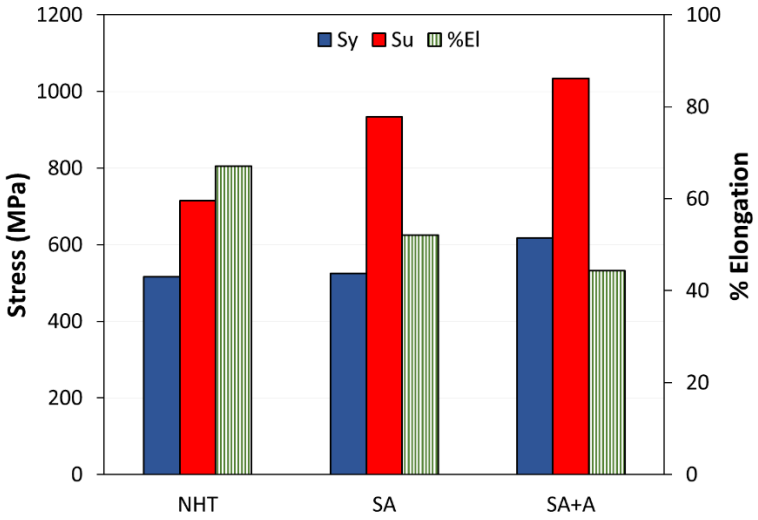

Figure 5. Summary of the tensile yield strength (Sy), ultimate tensile strength (Su), and the elongation to failure (% Elongation) for the NHT, SA and SA+A conditions.

The SEM fracture surface images for the NHT, SA and SA+A conditions are presented in Figure 6. In the NHT condition, large pores and dimples can be observed on the fractured surface. The reduction in area was measured to be 84% which correlates with the significant amount of plastic deformation during necking of the specimens. In comparison, for the SA and SA+A conditions, some cracks as well as dimples were observed on the fractured surfaces. For these two conditions, the reduction in areas were not as high as the NHT condition, however were still significant at 58% and 51% for the SA and SA+A conditions, respectively. Dimple fracture was seen in all of the conditions with a typical cup and cone fracture shape. This indicates that the fracture modes were ductile for all conditions with the tensile strengths being governed by the amount of solid solution strengthening as well as precipitation hardening from the respective heat treatments.

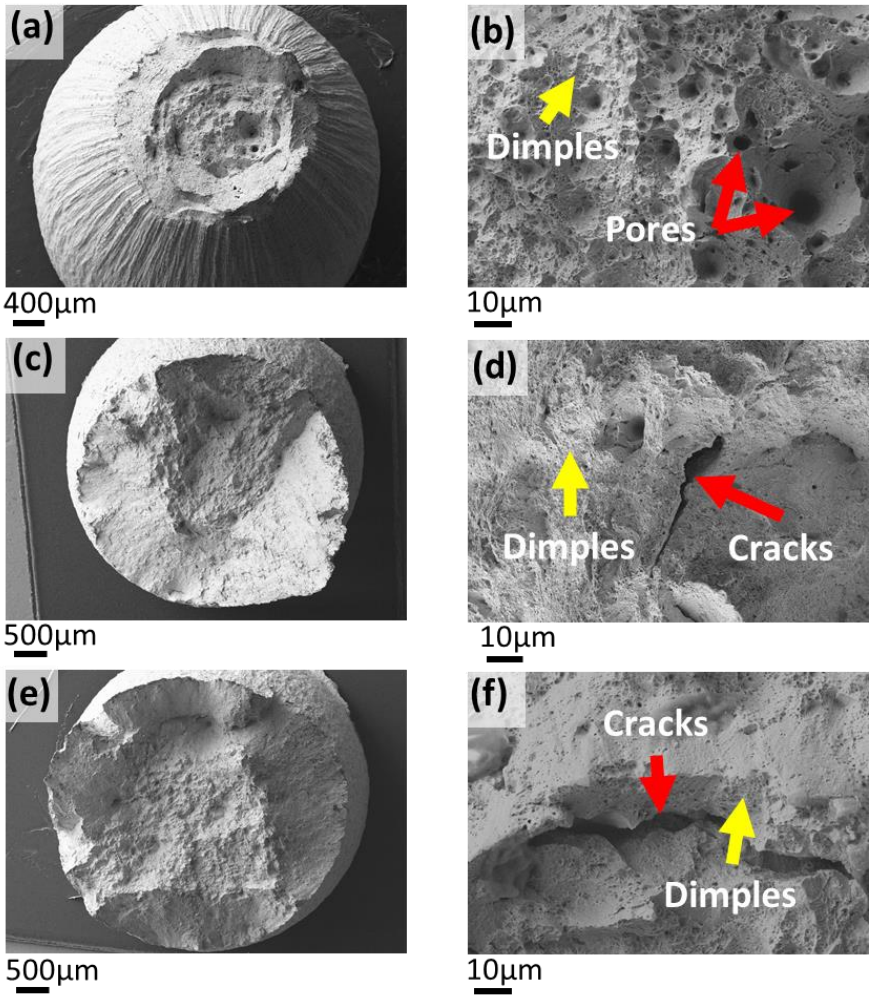

Figure 6. SEM images of fracture surfaces for the (a)-(b) NHT; (c)-(d) SA1100 and (e)-(f) SA+A conditions.

Conclusions

In this study, the effect of various heat treatments on the microstructure and mechanical properties of L-PBF Haynes 214 were investigated. A comprehensive microstructural characterization was carried out for various multi-step heat treatments which included SR, HIP, SA and SA+A. Grain growth was observed after SR treatment and no significant changes seen in the grain size/morphology upon subsequent heat treatments. BSE micrographs revealed a dendritic structure in the NHT condition, which dissolves after solution treatment. Fine γ' precipitates and grain boundary carbides started to form in the SA+A condition which resulted from the ageing step at 788°C for 8h. The highest tensile strengths were reported in the SA+A condition which was attributed to the formation of strengthening precipitates. The tensile fracture surfaces revealed that ductile failure occurred in all conditions with the highest elongation being measured for the NHT and the lowest in the SA+A condition.

Acknowledgment

This research is partially supported by the National Aeronautics and Space Administration (NASA) under Cooperative Agreement No. 80MSFC19C0010. This paper describes objective technical results and analysis. Any subjective views or opinions that might be expressed in the paper do not necessarily represent the views of the NASA or the United States Government.

References

[1] Pollock TM, Tin S. Nickel-based superalloys for advanced turbine engines: Chemistry, microstructure, and properties. Journal of Propulsion and Power 2006;22:361–74. https://doi.org/10.2514/1.18239.

[2] Sajjadi SA, Zebarjad SM. Study of fracture mechanisms of a Ni-Base superalloy at different temperatures. Journal of Achievements in Materials and Manufacturing Engineering 2006;18:227–30.

[3] Sabol GP, Stickler R. Microstructure of Nickel-Based Superalloys 1969;11.

[4] Hisazawa H, Terada Y, Takeyama M. Morphology evolution of γ′ precipitates during isothermal exposure in wrought Ni-based superalloy Inconel X-750. Materials Transactions 2017;58:817–24. https://doi.org/10.2320/matertrans.M2016376.

[5] Ghiaasiaan R, Poudel A, Ahmad N, Gradl PR, Shao S, Shamsaei N. High Temperature Tensile and Fatigue Behaviors of Additively Manufactured IN625 and IN718. Procedia Structural Integrity, vol. 38, Elsevier B.V.; 2021, p. 581–7. https://doi.org/10.1016/j.prostr.2022.03.059.

[6] Bsat S, Huang X, Penttila S. Corrosion behaviour of bare and nicraly coated alloy 214 in supercritical water at 700 C. Journal of Nuclear Engineering and Radiation Science 2018;4:1–5. https://doi.org/10.1115/1.4037324.

[7] Adegoke O, Andersson J, Brodin H, Pederson R. Review of laser powder bed fusion of gamma-prime-strengthened nickel-based superalloys. Metals (Basel) 2020;10:1–26. https://doi.org/10.3390/met10080996.

[8] Cieslak MJ, Stephens JJ, Carr MJ. A study of the weldability and weld related microstructure of cabot alloy 214. Metallurgical Transactions A 1988;19:657–67. https://doi.org/10.1007/BF02649280.

[9] Haynes International. HAYNES ® 214 ® alloy. https://haynesintl.com/docs/default-source/pdfs/new-alloy-brochures/high-temperature-alloys/brochures/214-brochure.pdf?sfvrsn=bf7229d4_30. 2021; [Brochure].

[10] Lee S, Ahmad N, Corriveau K, Himel C, Silva DF, Shamsaei N. Bending properties of additively manufactured commercially pure titanium (CPTi) limited contact dynamic compression plate (LC-DCP) constructs: Effect of surface treatment. Journal of the

Mechanical Behavior of Biomedical Materials 2022;126:105042. https://doi.org/10.1016/j.jmbbm.2021.105042.

[11] Schneider J. Comparison of Microstructural Response to Heat Treatment of Inconel 718 Prepared by Three Different Metal Additive Manufacturing Processes. Jom 2020;72:1085–91. https://doi.org/10.1007/s11837-020-04021-x.

[12] Rao K v, Herchenroeder RB. Microstructural characteristics of CABOT alloy No. 214, a new superalloy developed for applications in hostile, high-temperature environments. TMS (The Metallurgical Society) Paper Selection;(USA) 1984;56.

[13] Donachie MJ, Donachie SJ. Superalloys: a technical guide. ASM international; 2002.